Experimental Investigation of Regenerative Cooling Performance in Hybrid Rocket Engines

Giuseppe Gallo[1], Hiroki Kojima[2], Landon Kamps[3], Harunori Nagata[4]
Hokkaido University, Sapporo, Hokkaido, 060-8628, Japan

Abstract

An experimental investigation regarding the reliability and feasibility of a regenerative cooling system in hybrid rocket engines is presented. The novelty of the work is the introduction of a regeneratively cooled carbon-based nozzle throat using liquid oxidizer, for thermal management of the detrimental heat fluxes developed in the nozzle. The benefits and drawbacks of using regenerative cooling based on the observations of the current experimental campaign are critically discussed. Cryogenic oxygen in subcritical conditions is used as a coolant and oxidizer, for combustion with a fuel grain of high-density polyethylene stored within the combustion chamber. Pressure and temperature measurements are taken from multiple locations in the oxygen feed line and within the graphite nozzle throat. Eight firing tests were performed under various oxidizer mass flow rates and thus various thrusts. It was confirmed that cooling the graphite throat prevented the occurrence of nozzle erosion in all eight firing tests. The heat transfer rate and the physical state of the coolant are evaluated indirectly. Results show that increasing coolant gasification correlates with decreasing mass flow rate. The cooling performance improved more with higher vapour fractions than larger mass flow rates, however, dry-out occurred in tests with the highest gasification level. In summary, is it shown that while the current regenerative cooling system will supress nozzle erosion and limit nozzle temperatures in long duration firing, it reduces the predictability of flow rate and thus thrust during operations.

---

[1] JSPS International Fellow, Department of Space and Mechanical Engineering, and AIAA Member.

[2] Master's course student, Department of Mechanical and Space Engineering, and AIAA Member.

[3] Specially Appointed Assistant Professor, Department of Mechanical and Space Engineering, and AIAA Member.

[4] Professor, Department of Mechanical and Space Engineering, and AIAA Member.

Nomenclature

A	= area, m^2
c_p	= specific heat at constant pressure, J/kg·K
D	= inner nozzle diameter, m
D_{ext}	= external nozzle diameter, m
D_h	= hydraulic diameter, m
f	= skin friction coefficient
F	= heat transfer enhancement factor
G	= mass flux, kg/m^2·s
h	= heat transfer coefficient, W/ m^2·K
k	= thermal conductivity, W/ m·K
L	= length, m
$\dot{m}$	= mass flow rate, kg/s
N_{ch}	= channel number
Nu	= Nusselt number
OF	= mixture ratio
p	= pressure, Pa
P	= channel perimeter, m
Pr	= Prandtl number
$\dot{q}$	= heat flux per unit of area, W/ m^2
$\dot{Q}_x$	= heat flux per unit of length, W/ m
R	= universal gas constant
Re	= Reynolds number
t_b	= burning time, s
t_w	= nozzle thickness, m
T	= temperature, K
u	= velocity, m/s
w	= channel/fins width, m
X	= vapour quality
y	= radial coordinate

Greek Symbols

α	= void fraction
μ	= viscosity, kg/m·s
ρ	= density, kg/m^3

Superscripts

$\bar{}$	= time average

Subscripts

c	= coolant
conv	= convective
ch	= channel
dw	= downstream
f	= fuel
g	= gaseous
h	= hot
l	= liquid
m	= mixture
ox	= oxidizer
sat	= saturation
t	= throat
up	= upstream
v	= vapour
w	= wall

Abbreviations

HRE	= hybrid rocket engine
HDPE	= high-density polyethylene
LOX	= liquid oxygen
TPS	= thermal protection system

1 Introduction

Hybrid rockets (HREs) have become one of the most researched propulsion systems, largely due to their combination safety and simplicity [1, 2]. Similar to solid rockets, hybrid rockets' thrust chambers do not require active cooling because the solid fuel works as an insulator between the hot combustion gas and the metallic case. Most developers also opt not to use expensive and complicated active cooling systems in critical zones such as the nozzle throat, relying on carbon-based materials for thermal protection. However, some critical issues, such as nozzle erosion, need to be addressed in order to make hybrid rockets more competitive than existing solid rocket motors and liquid rocket engines. Nozzle erosion refers to the degradation and regression of the inner surface of a carbon-based nozzle as a result of chemical reactions with the combustion gas flowing through it [3,4]. It occurs when the combusting mixture is rich in oxidizing species and the temperature of the nozzle wall is sufficiently high to promote heterogeneous chemical reactions with these oxidizing species [5,6,7,8,9]. Hence, the nozzle cooling below the activation temperature allows the suppression of nozzle erosion.

Furthermore, passively cooled nozzles introduce the risk of overheating of spacecraft in certain in-space propulsion applications, which typical require a limited exchange surface area as well as burning times over 1 minute. No heat transfer mechanisms are available in space to discharge the energy transferred from the nozzle to the motor structure, which could go back to the satellite payload and electronics. Based on the authors' experience, passively cooled nozzles become one of the heaviest parts of the propulsion system because they require thick thermal protection systems (TPS) to be employed for thermal insulation. In summary, regenerative cooling equips hybrid rockets with two innovative features: 1. the capability for the motor to self-regulate heat fluxes produced within the nozzle without any external cooling or thermal protection system; 2. the improvement of the specific impulse through nozzle erosion suppression.

Regenerative cooling is widely used in liquid rocket engines for the cooling of the thrust chamber. Fuels are usually used as coolant because of their superior cooling properties than oxidizers [10]. Much research has been conducted on cooling systems employing hydrocarbon fuels with the aim to understand and limit the sooth production by endothermic pyrolysis in high pressure and temperature environments [11,12]. Film cooling is also employed as an option for the dilution of the boundary layer and the reduction of the heat fluxes, when fuels are available in liquid or gaseous phase [13]. Oxidizers, which are generally considered to have inferior cooling capabilities, are the only available propellants in the liquid phase in hybrid rockets. Nonetheless, there are a sufficient number of examples in open literature that show regenerative cooling using oxidizers is possible. One of these reports is by Price, who successfully cooled the nozzle throat in copper of a liquid rocket engine using liquid oxygen (LOX) [14]. A similar effort was made by Yuasa et al. with the further goal of vaporizing the liquid oxygen before the injection in the main chamber of a hybrid rocket [15]. Another example is a 1U CubeSat-sized hybrid rocket plug nozzle cooled by nitrous oxide [16]. In all cases, metallic nozzles with internal coolant paths were used. An additional novelty introduced by the authors in this study is the employment of graphite nozzles in an active cooling system. The main advantage is the redundant safety of using an ablative material; simply put, cooling a graphite nozzle throat increases the safety and reliability of the system because the risk of catastrophic failure in the case of anomalous overheating, etc., is mitigated down to a risk of minor performance loss resulting from nozzle erosion.

In this scenario, an experimental campaign on a 30 N hybrid rocket engine equipped with regeneratively cooled graphite nozzle throat was carried out at the Hokkaido University Laboratory of Space Systems. Different operating conditions have been explored by increasing the LOX tank pressure step by step, which is the main controlling parameter of the feeding system. This paper illustrates the benefits and drawbacks of using regenerative cooling in subcritical conditions observed in our experiments. The cooling performance of cryogenic oxygen was investigated and discussed, revealing counter-intuitive results.

In particular, the convective heat transfer was dominated more so by multiphase effects than by flow rate. Simply put, the best cooling performance was achieved in highly gasified tests rather than in tests with the large mass flow rates. However, dry-out was observed for tests with the highest gasification rates, leading to poor cooling performance and detrimental nozzle temperatures.

In summary, an experimental study of the performance of regenerative cooling system in hybrid rockets is the main objective of the current paper. The novelty of the work lies in the introduction of cooling systems in HREs, which usually relied on passive thermal protection systems for the insulation of the nozzle from the metallic case. The paper consists of three main sections. Firstly, the experimental set-up is described, including the data reduction techniques used to calculate the most interesting heat transfer and multiphase quantities, such as the cooling heat transfer coefficient and the average vapour quality/void fraction. Secondly, the measured and computed experimental data are shown and discussed with a focus on nozzle erosion suppression. Finally, the characteristic multiphase regime developed in the cooling channels is identified with estimations of the average void fractions and vapour quality. The performance of the cooling system is evaluated by measuring the coolant heat transfer coefficient at different coolant mass flow rates.

2 Experimental Setup and Data Reduction Technique

This section describes the test apparatus and the hybrid rocket motor configuration. Figure 1 shows a simplified diagram of the experimental apparatus employed for the firing tests. The fuel and the oxidizer employed in the firing tests are high-density polyethylene and oxygen, respectively. As is evident in the schematic, there is a single liquid oxygen supply line, such that the liquid oxygen is used to cool the graphite rocket nozzle before being injected into the main combustion chamber. The cryogenic liquid oxygen is pressurized in the tank and supplied to the cooling channels by a high-pressure helium tank placed upstream of the liquid oxygen reservoir, which maintains the coolant temperature between 110 and 120 K.

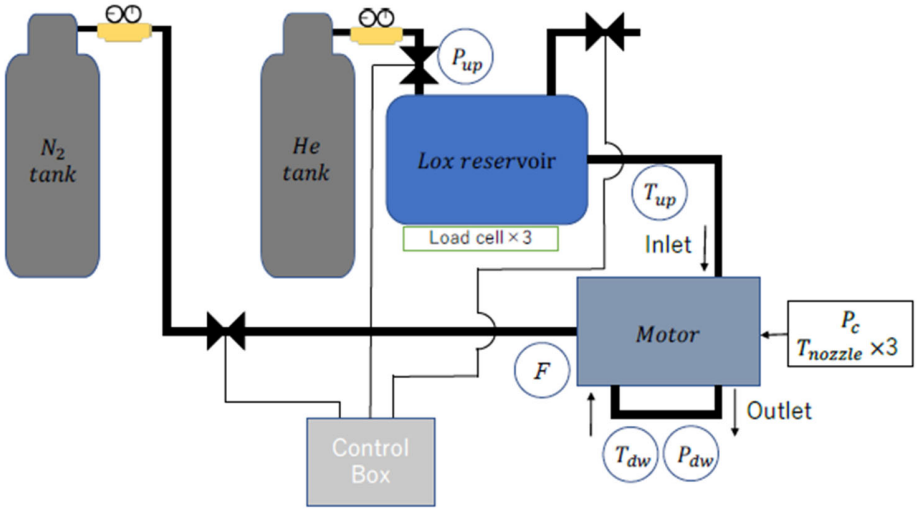

Figure 1 Schematic of the apparatus used for the experimental tests.

The authors decided to implement a valveless supply system to simplify the regenerative cooling line. In this way, expensive cryogenic valves are avoided, and the coolant injection in the feed pipe is controlled by the upstream pressure, as shown in Figure 2. Two cylindrical walls divide the inside tank volume, forming an internal pressure-driven circuit. When the motor is off-operation, the external part of the volume is connected to the internal part because, in the case of the oxygen,

the vapour released by the liquid oxidizer may produce a differential pressure pushing the oxidizer in the feed system; on the other hand, when the motor is ready for the firing test, the external side is connected to the pressurizing tank, providing the feed pressure for oxidizer supply [17].

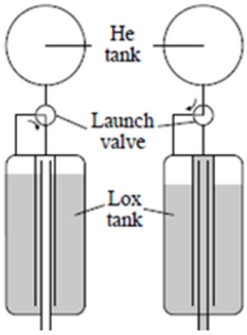

Figure 2 Valveless LOX feed system.

An additional nitrogen tank is included in the main line for purging the motor after combustion. The gaseous and liquid oxygen tanks are placed on load cells, which measure the mass loss of the reservoir during the burn. Figure 3 shows a representation of the motor assembly and the concept of regenerative cooling. The cryogenic oxygen supplied from the pressurized reservoir flows through the cooling system, which consists of three helical channels wrapped around the external diameter of the graphite nozzle. The pressure and temperature are recorded upstream and downstream of the cooling system in order to measure the pressure drop and temperature rise before the injection into the chamber. An additional pressure measurement is taken upstream of the chamber (named p_{inj} in Figure 3). The pressures are measured with three Kyowa PHB-A transducers with an instrument measurement error of $\pm 5 \cdot 10^3$ Pa. The temperature is measured by a K-type thermocouple with an error of ± 5°C. Furthermore, the rocket is placed in front of a Kyowa LMB-A-50N class load cell for the measurement of the thrust with an error of ± 0.30 N. Three load cells are also employed for the measurement of the tank weight during the burning time for the evaluation of the average mass flow rate with a measurement error of ± 0.22 N. The time-averaged oxidizer mass flow rate is then obtained by the time derivative of the linear best fit. The analogue signals generated by thermocouples, pressure transducers, and load cells are sampled at 200 Hz, digitally converted, processed, and recorded on the hard disk by a Kyowa universal recorder EDX-100A standard system interconnected with the computer by means of fiber optic connections. Finally, the fuel consumption, essential for the evaluation of the average mixture ratio and the characteristic velocity, is estimated by measuring the fuel grain weight before and after the firing test on a digital scale with an error of ± 1 g.

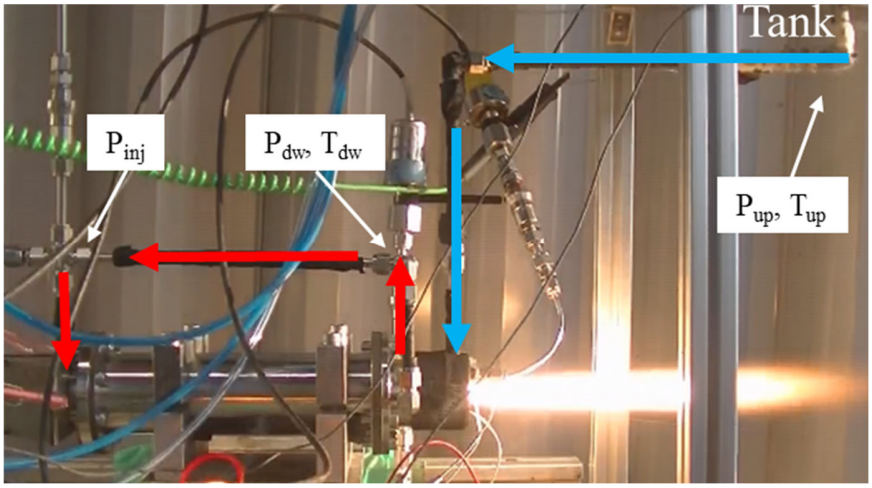

Figure 3 Snapshot of a video taken during a firing test with a representation of the regenerative cooling flow path; (blue arrows, cryogenic coolant path; red arrows, gasified coolant path).

A graphite nozzle is used in the tests, which has three holes for inserting sheath-type thermocouple leads, by which nozzle temperatures were measured at 3, 5, and 7 mm from the inside surface of the throat section. The nozzles used in all tests were manufactured using the same grade of isotropic graphite (G347; Tokyo Tokai Carbon, Ltd.). The density and thermal conductivity at atmospheric conditions are listed by the manufacturer to be $\rho_n = 1850$ kg/m^3 and $k = 116$ W/(m·K), respectively [18]. The nozzle length is 60 mm, and the throat is located in the middle. The convergent inlet section, the throat, and the exit section have a diameter of 30 mm, 6 mm, and 14 mm, respectively. The external diameter (around which the channels are wrapped) is 36 mm. The nozzle is mounted within a metallic case containing three helical fins with a width and height of 1 mm, which travel around the nozzle axis with a rotation angle of around 3 degrees. Differently from our previous work, the nozzle length featured by helical channels is long 24 mm placed symmetrically with the throat, consequently the helical angle is around 3 degree and the channel length around 452 mm. The channels have been manufactured by a 3D printer; the current channel dimensions represent the lower manufacturing limit of the printer. Therefore, three helical channels are obtained from the accommodation of the nozzle into the metallic case. The choice of the number of channels was deeply discussed in our previous work [19]. The coolant flows in the opposite direction from the exhausting gases. The heated coolant is gathered in a collector at the channels' end and injected into the main chamber by a pipe. Figure 4 represents the described assembly.

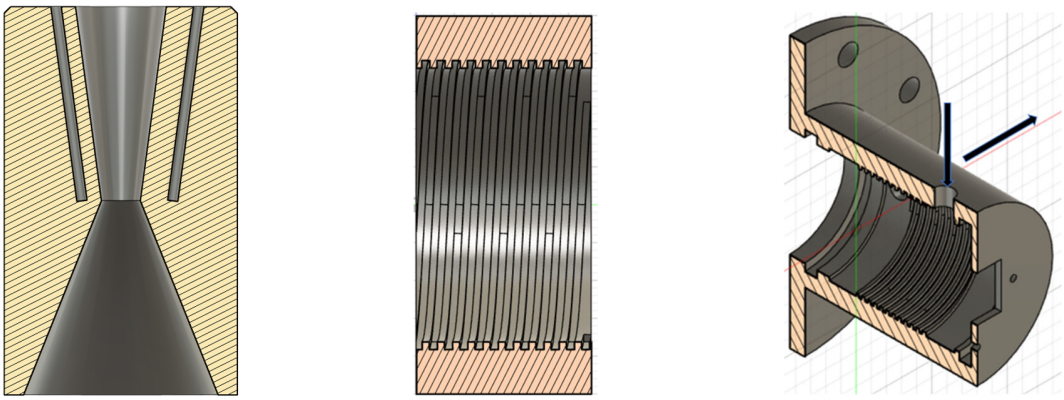

a) Graphite nozzle. **b) Helical channels.** **b) External case.**

Figure 4 Details of graphite nozzle insert and the metallic case.

The evaluation of the nozzle erosion is performed using image techniques. Initial and final nozzle throat diameter measurements were taken by analysing digital photographs of the nozzle before and after firing using ImageJ [20]. These photographs were taken at 40X digital zoom from a distance of 2 m from the nozzle throat. A length scale was established for the scan by placing a plaque of 1-mm-spacing grid paper next to the nozzle being scanned. This procedure was repeated five times before and after each firing test, and the standard deviation of these measurements was incorporated into the uncertainty of this measurement; however, the standard deviation of measurements was typically much smaller than the uncertainty of the length scale. The length scale uncertainty was assumed to be two times the thickness of a grid line (0.2 mm).

2.1 Data Reduction Technique

2.1.1 Propulsion and Multiphase Quantities

In this subsection, all the equations used for data reduction of experimental results are shown. First, the burning time has been computed, starting from half of the pressure rise to half of the final pressure drop. The average fuel mass flow rate and mixture ratio are calculated from the fuel grain mass loss and the burning time, as:

$$\overline{\dot{m}_{\mathrm{f}}} = \frac{\Delta \mathrm{M}_f}{t_b}$$
$$\overline{OF} = \frac{\dot{\mathrm{m}}_{ox}}{\overline{\dot{m}_{\mathrm{f}}}} \tag{1}$$

The space averaged density of the coolant along the channels can be evaluated from the Darcy–Weisbach equation, by:

$$\bar{\rho} = \frac{f}{2} \frac{\dot{\mathrm{m}}_{ox}^2}{(p_{up} - p_{dw})} \frac{L_{ch}}{A_{ch}^2 D_h} \tag{2}$$

Where L_{ch} and A_{ch} are the length and the area of the channel, D_h is the hydraulic diameter defined as $D_h = 4A_{ch}/P_{ch}$ with P_{ch} the channel perimeter, p_{up} and p_{dw} are the pressures upstream and downstream of the cooling system (their difference represents the pressure jump, Δp) and f is the so-called friction factor. Note that Eq. (2) is usually used for the evaluation of f. However, the results displayed in the next sections show that the jump pressure is controlled by the boiling of the liquid oxygen in the channels.

The friction coefficient is also unknown, and it is extremely tricky to evaluate for multiphase flows because it depends on many factors, such as: 1. Definition of the channel roughness; 2. Evaluation of the amount of gasified coolant; and, 3. Definition of the multiphase flow regime. In our test cases, the liquid Reynolds number varies between $2.6 \cdot 10^4$ and $6.2 \cdot 10^4$, meaning that the multiphase regime can be assumed to be turbulent and homogeneous. A rough estimation can be done by using the modified Moody chart for homogeneous multiphase flows, which is represented by the following equation [21]:

$$\frac{1}{\sqrt{f}} = 3.48 - 4\log_{10}\left(\frac{2\varepsilon}{D_h} + \frac{9.35}{Re_m\sqrt{f}}\right) \tag{3}$$

Where ε is the channel roughness and Re_m is the mixture Reynolds number defined:

$$Re_m = \frac{G_{ox} D_h}{\mu_m} \tag{4}$$

$$\mu_m = \alpha\mu_v + (1-\alpha)\mu_l$$

Where G_{ox} is the oxidizer mass flux, μ_m is the mixture viscosity and α is the void fraction. Note that the subscripts v and l refer to the oxygen values at the vapor and liquid states, respectively. Figure 5 represents the friction factor for different Re_m and ε/D_h .

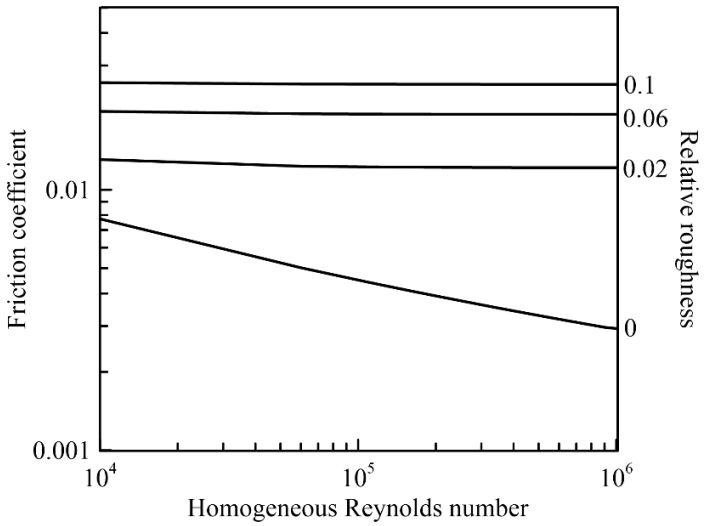

Figure 5 Modified Moody chart for homogeneous multiphase flows obtained by Eq. (3).

For Re_m representative of our tests, i.e., higher than $2 \cdot 10^4$, f is approximately constant for a reasonable value of relative roughness and unrelated to the homogeneous Reynolds number. Imposing a reasonable ε/D_h equal to 0.1, a reference value of the friction coefficient of around 0.025 is computed. It is worth noticing that while the choice of the friction coefficient affects the quantitative calculation of the interested quantities, it is irrelevant to the results from a qualitative point of view. However, for researchers interested in the development of numerical models based on the results of this work, the quantitative results are still valid if the friction coefficient is modelled by Eq. (3) with $\varepsilon/D_h = 0.1$.

Once f is fixed and $\bar{\rho}$ is computed, the average void fraction, $\bar{\alpha}$, and the average vapor quality, $\bar{X}$, are given by:

$$\begin{aligned} \bar{\alpha} &= \frac{\rho_l - \bar{\rho}}{\rho_l - \rho_v} \\ \bar{X} &= \frac{\bar{\alpha}\rho_l}{(1-\bar{\alpha})\rho_v(\bar{p},\bar{T}) + \bar{\alpha}\rho_l} \\ \bar{p} &= \frac{p_{up}+p_{dw}}{2}, \quad \bar{T} = \frac{T_{up}+T_{dw}}{2} \end{aligned} \tag{5}$$

$\bar{\alpha}$ and $\bar{X}$ are crucial quantities because they allow the evaluation of the average mixture properties, such as the viscosity and the specific heat:

$$\begin{aligned} \mu_m &= \bar{\alpha}\mu_v(\bar{p},\bar{T}) + (1-\bar{\alpha})\mu_l \\ c_{pm} &= \bar{\alpha}\rho_v c_{pv}(\bar{p},\bar{T}) + (1-\bar{\alpha})\rho_l c_{pl} \end{aligned} \tag{6}$$

The vapour thermodynamic quantities are evaluated by Modified-Benedict-Webb-Rubin (MBWR) equation of state for real gas developed by Younglove [22,23], while the transport properties are evaluated by the approach of Hanley et al. [24]. Figure 6 represents the typical contours obtained for the oxygen density and dynamic viscosity for any pressure, temperature and fluid state. The inlet coolant conditions are closer to the saturation line than the outlet states. For this reason, the liquid quantities are assumed to coincide with the saturation ones at the upstream pressure.

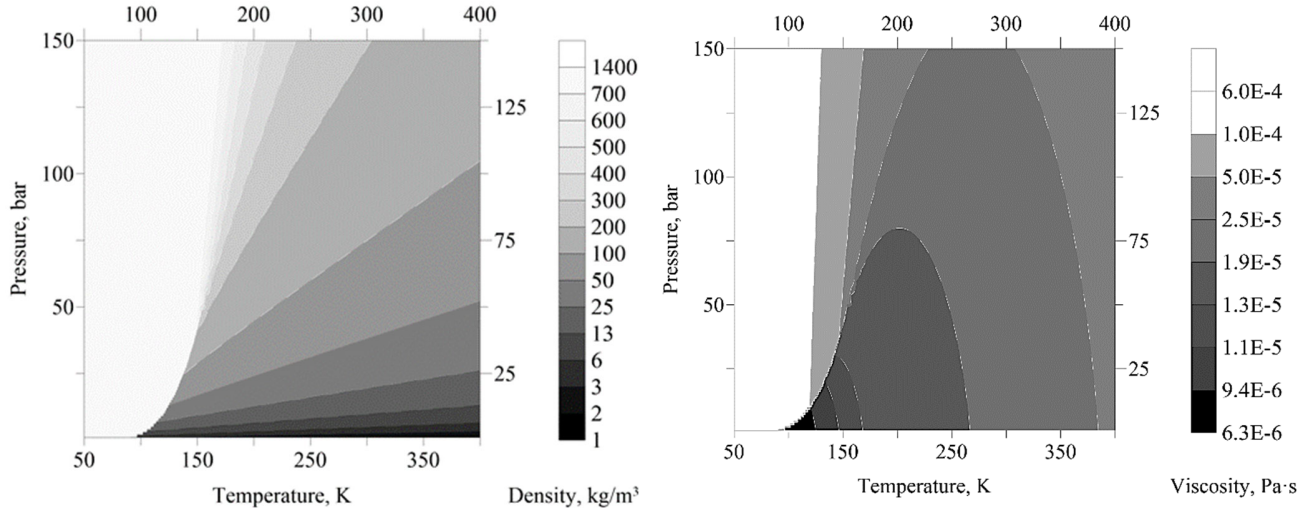

(a) Density. **(b) Dynamic viscosity.**

Figure 6 Contours of the coolant density and the dynamic viscosity varying pressure and temperature.

2.1.2 Heat Transfer Quantities at the Throat

In this subsection, the methodology used for the evaluation of the coolant heat transfer coefficient, h_c, the hot gas heat transfer coefficient, h_g, and the heat flux per unit of length, $\dot{Q}_x$, is described. Heat is transferred from the hot-gas (subscript g) to the coolant (subscript c) via the solid wall of the graphite nozzle as shown in Figure 7.

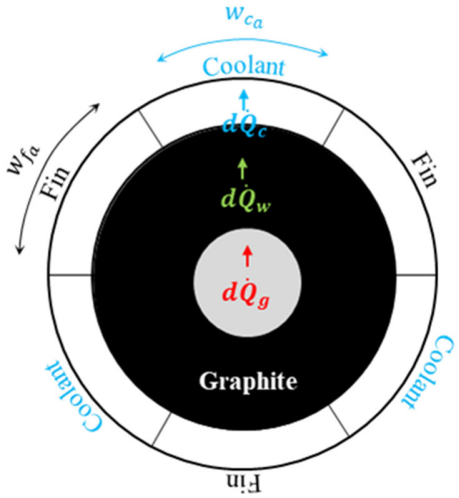

Figure 7 Schematic of heat transfer path from hot gases to cooling channels.

The one-dimensional model relies on the heat transfer balance between hot gas, wall, and coolant for steady-state conditions. The hot-gas heat transfer rate by convection affects the wall ($\dot{Q}_{g,x}$), is transmitted by conduction through the wall ($\dot{Q}_{w,x}$), and is transported by convection to the coolant ($\dot{Q}_{c,x}$). For steady-state conditions, these heat transfer rates must be equal:

$$\dot{Q}_x = \dot{Q}_{g,x} = \dot{Q}_{w,x} = \dot{Q}_{c,x} \tag{7}$$

Where $\dot{Q}_x$ is the heat transfer rate per unit of length. At the steady state in correspondence of the throat section, the terms in the above heat balance equation are given by:

$$\dot{Q}_{g,x} = \pi D_t h_g (T_0 - T_{wh}) \tag{8}$$

Where D_t is the throat diameter, T_{wh} is the nozzle temperature at the throat from the hot side, while T_0 is the adiabatic wall temperature, which coincides with the flame temperature assuming a unitary recovery factor. The flame temperature is calculated by chemical equilibrium calculations assuming liquid oxygen at the temperature T_{dw} and high-density polyethylene (HDPE) at the corresponding average mixture ratio. Note that h_g, evaluated by Eq. (8), also includes uncertainty regarding the deviation of the experimental temperature from the equilibrium combustion temperature corresponding to the experimental average mixture ratio. On the coolant side, the following relation is valid:

$$\dot{Q}_{c,x} = \frac{\pi D_{ext}}{2} h_c (T_{wc} - T_c) \tag{9}$$

Where D_{ext} is the external nozzle diameter, T_{wc} is the nozzle temperature at the coolant side, while T_c is the coolant temperature at the throat, which is assumed equal to $\bar{T}$ of Eq. (5). It is worth noticing that the wet surface πD_{ext} is divided by 2 in order to take into account the presence of the fins, as displayed in Figure 7. This is true, assuming that the lateral walls of the channel are adiabatic.

Regarding the heat conduction through the solid nozzle, the 1D Fourier's law of heat conduction for heat transfer through a cylindrical layer with non-negligible thickness is expressed as

$$\dot{Q}_{w,x} = \frac{2\pi k_s(T)}{\ln (D_{ext}/D_t)} (T_{wh} - T_{wc}) \tag{10}$$

Where k_s is the graphite thermal conductivity, which, in turn, depends on the nozzle temperature. Therefore, from Eq.(10) the following expression can be obtained

$$T(y) = T_{wh} - \frac{\dot{Q}_x}{2\pi k_s(T)} \ln (D(y)/D_t) \tag{11}$$

Where y is the nozzle radial coordinate at the throat. Let us give an example of how to use Eq. (11). As stated above, the nozzle temperatures are recorded at 3, 5 and 7 millimeters from the throat; hence the corresponding non-dimensional diameters, $D(y)/D_t$, are equal to 2, 2.67, 3.33, respectively. Plotting the steady state temperatures against the non-dimensional diameters and computing the logarithmic best-fit trend-line, an equation similar to Eq. (11) can be obtained. In the particular case of Figure 8, the equation is

$$T(y) = 754 - 150.8 \ln (D(y)/D_t) \tag{12}$$

Where:

- T_{wh} is immediately evaluated, and it is equal to 754 K;
- T_{wc} is around 515 K, and it is obtained by evaluating the regression law at $D(y)/D_t$ equal to 6;
- $\dot{Q}_x$ is assessed by multiplying 150.8 by $2\pi k(T)$. The thermal conductivity of the graphite was evaluated at the average temperature of the radial profile. The dependence of the graphite properties on temperature is taken into account following Ref. [25], whose profile of thermal diffusivity and conductivity are shown in Figure 9.

Once obtained these three quantities, h_g and h_c are given by Eq. (8) and Eq. (9).

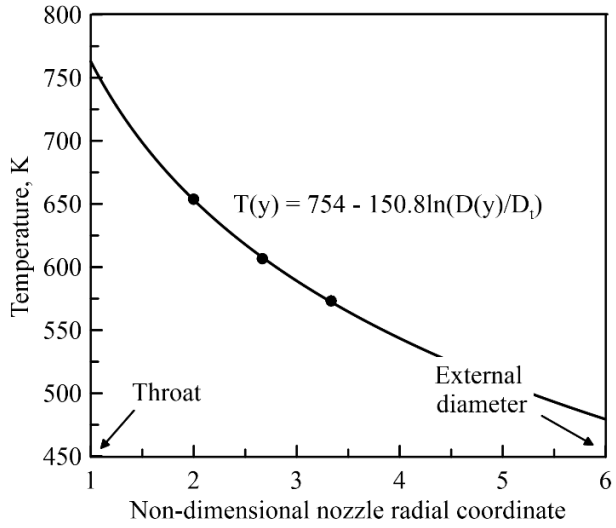

Figure 8 A representation of a typical experimental temperature profile along the nozzle thickness at the throat.

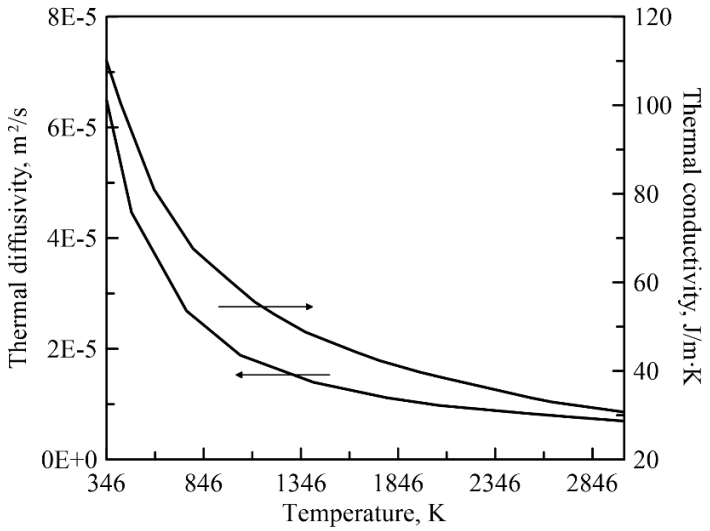

Figure 9 Graphite thermal properties with density equal to 1850 kg/m^3.

3 Experimental Results

This section presents the main experimental findings of the firing test campaign. Firstly, a typical firing test during the burning time is shown and compared with a test at different mass flow rates; secondly, all the quantities regarding the phase change are displayed and discussed; finally, the results regarding the heat transfer are given.

3.1 Typical Experimental Test and Measured Results

The experimental campaign consists of eight firing tests, in which nozzle erosion was successfully suppressed. The measured data collected during the burning time has been listed in Table 1. The data are sorted by increasing the value of the tank pressure. The inlet temperature is approximately constant, around 116 K, so the operating conditions are expected to be mainly sensitive to the tank pressure.

Table 1 Experimental measured results.

Test	Upstream pressure, bar	Upstream temperature, K	Coolant mass flow rate, g/s	Mixture ratio	Thrust, N	Specific Impulse, m/s	Downstream pressure, bar	Downstream temperature, K	Injection pressure, bar
1	20.2 ± 0.05	117 ± 5	7.9 ± 1.31	1.68± 0.29	18.1 ± 0.30	1428 ± 108	10.0 ± 0.05	373 ± 5	9.1 ± 0.05
2	20.7 ± 0.05	117 ± 5	8.0 ± 1.19	1.38± 0.36	27.2 ± 0.30	1956 ± 296	13.6 ± 0.05	331 ± 5	11.8 ± 0.05
3	23.0 ± 0.05	116 ± 5	13.7 ± 1.49	2.32± 0.27	30.1 ± 0.30	1536 ± 121	13.7 ± 0.05	301 ± 5	12.7 ± 0.05
4	24.3 ± 0.05	116 ± 5	11.5 ± 1.51	2.06± 0.26	34.3 ± 0.30	1923 ± 161	15.0 ± 0.05	258 ± 5	13.7 ± 0.05
5	24.6 ± 0.05	115 ± 5	12.0 ± 1.52	2.01± 0.23	33.5 ± 0.30	1793 ± 158	13.7 ± 0.05	314 ± 5	13.4 ± 0.05
6	24.7 ± 0.05	115 ± 5	15.5 ± 1.50	2.38± 0.29	34.1± 0.30	1545 ± 155	13.7 ± 0.05	319 ± 5	12.5 ± 0.05
7	26.0 ± 0.05	116 ± 5	16.8 ± 1.48	2.4± 0.36	35.3 ± 0.30	1470 ± 148	15.0 ± 0.05	331 ± 5	14.1 ± 0.05
8	27.5 ± 0.05	115 ± 5	18.6 ± 2.28	2.5± 0.26	41.9 ± 0.30	1615 ± 109	16.7 ± 0.05	290 ± 5	15.2 ± 0.05

Test	Nozzle temperature at 3 mm, K	Nozzle temperature at 5 mm, K	Nozzle temperature at 7 mm, K
1	579 ± 5	551 ± 5	538 ± 5
2	659 ± 5	-	620 ± 5
3	622 ± 5	571 ± 5	532 ± 5
4	800 ± 5	761 ± 5	731 ± 5
5	623 ± 5	-	582 ± 5
6	637 ± 5	590 ± 5	555 ± 5
7	674 ± 5	607 ± 5	573 ± 5
8	673 ± 5	617 ± 5	602 ± 5

- Thermocouple failure.

First, a typical firing test is described here. Test 6 is taken as an example. Figure 10a represents the coolant jump pressure and the temperature rise through the cooling system, while Figure 10b represents the temperatures measured along the nozzle thickness during the test at 3, 5, and 7 millimeters from the throat inner surface. Two transients are recognized during the burning time in Figure 10b:

- Time duration of 0 – 11 s: the nozzle was heated by the combustion gas, and the coolant physical state evolved towards the steady state condition. During this time, the inlet coolant conditions remained constant during the burning time, the outlet temperature rose from 187 K to 331 K, and the outlet pressure dropped from around 21 to 16 bar. Consequently, the pressure drop increased from 5 to 10 bar, suggesting that the coolant density was largely decreasing due to the gasification.
- Time duration of 11 – 17 s: the sudden nozzle heating observed in the first 11 s was dampened by the cooling system. The temperature drops along the nozzle thickness followed the logarithmic law described by Eq. (10). The coolant state reached a steady multiphase state along the channel. However, the nozzle took additional time to adjust to the final cooling performance.

The length of the nozzle thermal transient depends on the thickness, which is large in this specific application.

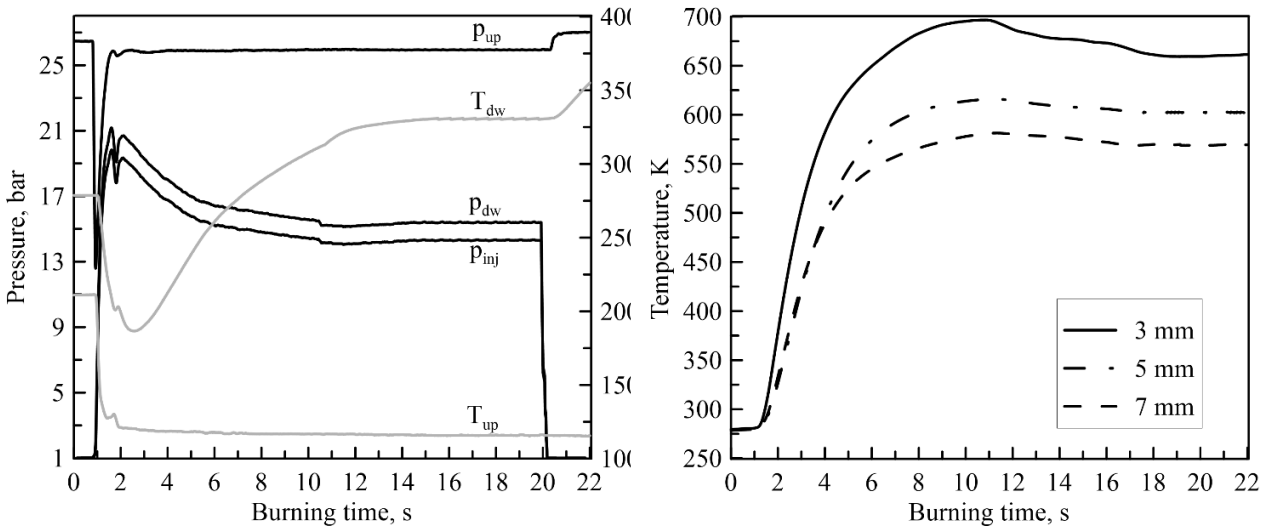

(a) Jump pressure and temperature raise. **(b) Nozzle temperatures.**

Figure 10 A representation of the pressure drop and temperature rise through the channels and nozzle temperatures measured at 3, 5, and 7 mm from the throat inner surface in Test 7.

Figure 11 compares the operative conditions of Test 2 and Test 8, which exhibited mass flow rates of 8 and 18.6 g/s, respectively. The inlet coolant temperature is equal in both tests, and the inlet pressure is 7 bar higher in Test 8. The pressure jumps through the cooling system are roughly 8 and 10 bar, respectively. An additional jump pressure is recorded between the outlet of the cooling system and the downstream transducer placed near the chamber. Coolant heating values of 219 and 184 K downstream of the cooling system are measured during the firing tests, respectively, while steady state temperatures of 660 and 670 K are observed at three millimetres from the throat. Finally, Figure 11c displays the motor thrust during the tests; at the steady state, the thrust of Test 8 increased by 60% compared to Test 2, although the mass flow rate was higher by 132%. Therefore, the specific impulse, in particular the characteristic velocity, decreased among the two tests.

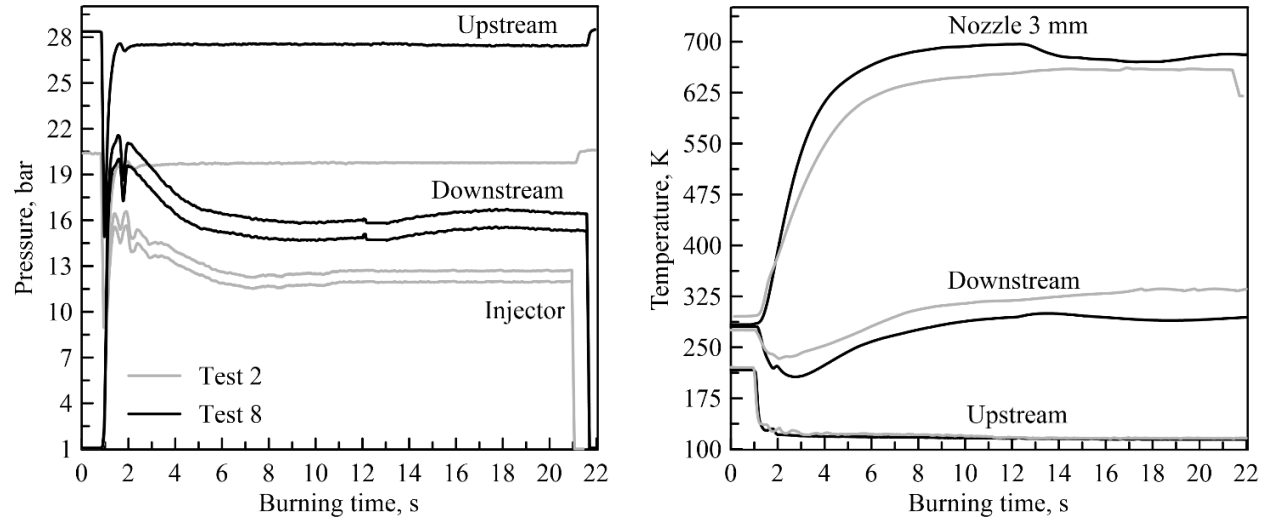

(a) Pressure cascade. **(b) Nozzle temperature and coolant temperature rise.**

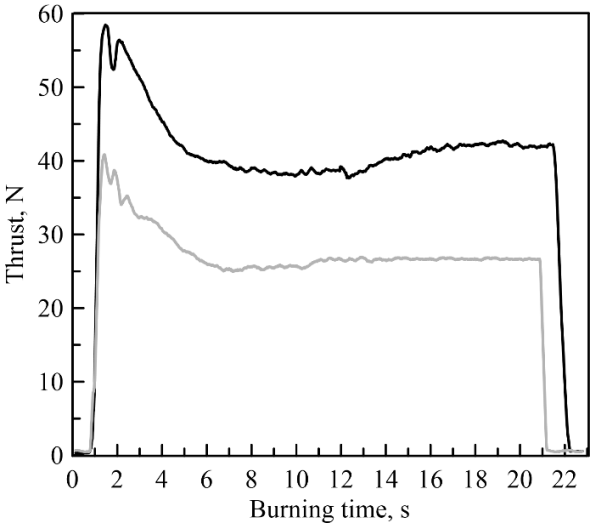

(c) Thrust.

Figure 11 Comparison of the coolant pressure cascade and temperature rise along the feed line, nozzle temperature and thrust between Test 2 with Test 8.

Figure 12a shows the chain of jump pressures registered along the feed line. The most significant drop is observed along the cooling channels, whose length is around 1.13 m. An additional drop of around 1 bar is also measured between the channel outlet and the transducer near the combustion chamber. The pressure drop along the cooling system is approximately constant, around 10 bar, with some fluctuations due to the relation of the pressure cascade with the chamber pressure (and the motor combustion efficiency). Figure 12b displays the achieved mass flow rates among the firing tests. It increases with the tank pressure, while a weak correlation is observed with the jump pressure with a power of 0.24. Rearranging Eq. (2), one can obtain:

$$\dot{m}_{ox}^2 = \frac{2}{f}\frac{(p_{up} - p_{dw})}{\bar{\rho}}\frac{A_{ch}^2 D_h}{L_{ch}} \tag{13}$$

Which shows that the mass flow rate is also related to the density variations due to the coolant gasification. This issue is deeply discussed in the next subsections. Figure 12c displays the motor thrust with the total mass flow rate, which linearly increases from 18 to 42 N. The specific impulse ranges between 1500 and 2000 m/s. Figure 12d displays the temperatures recorded at the inlet and outlet of the cooling system. The inlet temperature is approximately constant among the tests, while the outlet temperature seems to decrease, increasing the mass flow rate. Note that the coolant temperature is related to the amount of heat flux provided by the combustion gases and the capability of the coolant to absorb energy from the nozzle wall, which is discussed in the next section. Test 4 is of particular interest, in which the temperature rise was especially low, around 142 K. Accordingly, the temperatures registered along the radial nozzle coordinate for this test, which are shown in Figure 12e, are dramatically high, with a peak of around 800 K for the thermocouple placed at 3 mm from the inner throat surface. In all the other tests, the maximum temperature is below 700 K, proving the cooling system's capability to suppress nozzle erosion.

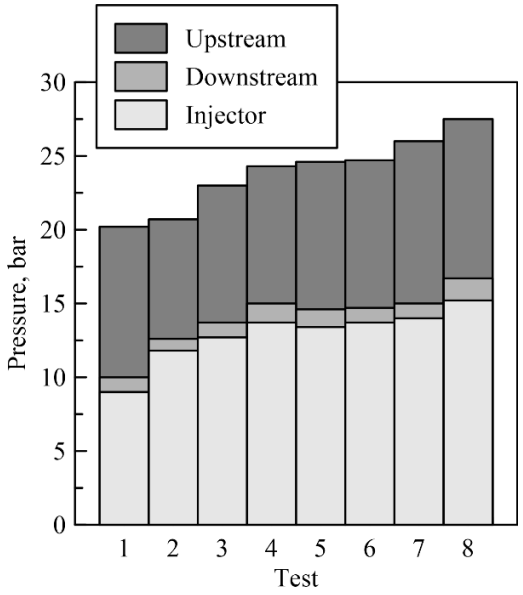

(a) Upstream, downstream and injection pressure.

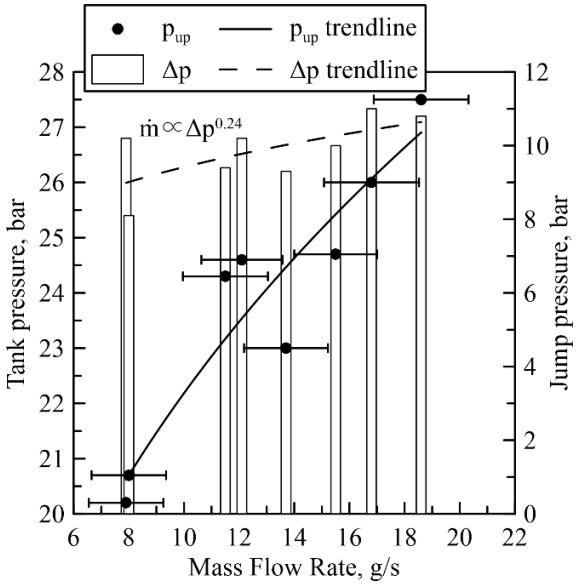

(b) Tank and jump pressure vs mass flow rate.

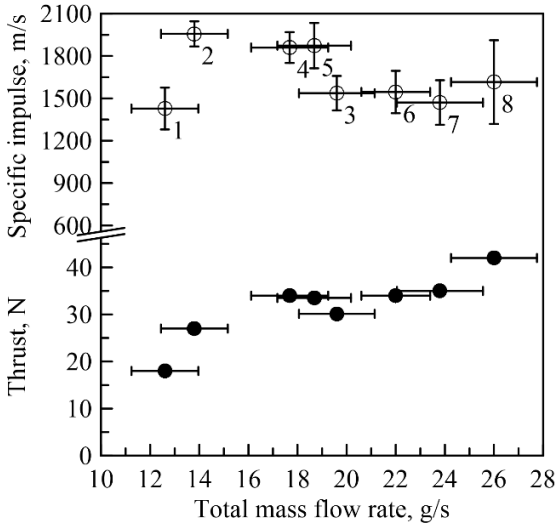

(c) Motor thrust vs injection pressure.

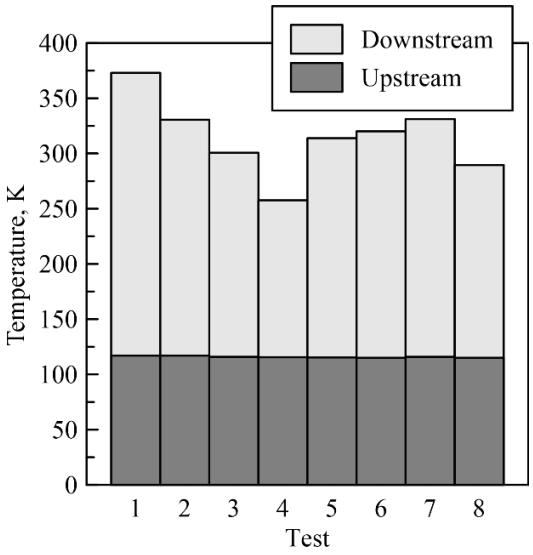

(d) Upstream and downstream temperature.

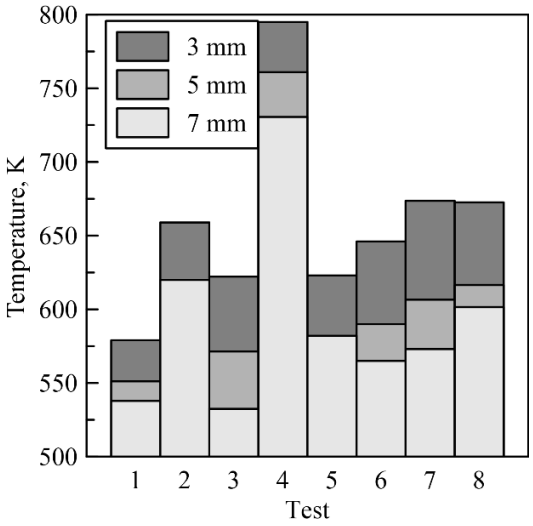

(e) Temperatures at 3, 5 and 7 mm from the throat inner surface.

Figure 12 A representation of the main quantities recorded in the experimental campaign.

3.2 Nozzle Erosion Suppression and Thermal Management

In this section, the effective suppression of nozzle erosion by implementing a regenerative cooling system is discussed. The idea of regenerative cooling was conceived of after performing previous experimental campaigns in which nozzle erosion was observed in 44 tests for many motor configurations and operative conditions comparable to those considered in this work [8]. Figure 13 represents the image analysis of one of the 44 tests (Test DNT-2) before and after the firing test. Although the nozzle diameter is 2 mm smaller than the current configuration, the pressure and throat mass fluxes are roughly equivalent to the presented firing tests. A throat enlargement from 4 to 6 mm is displayed, giving evidence of the detrimental effect of the nozzle configuration in small motors.

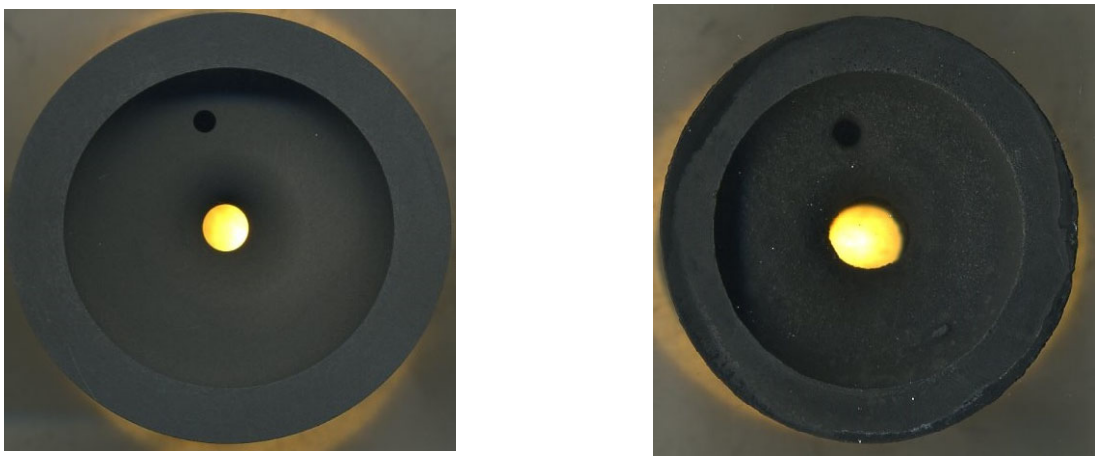

(a) Before the firing test. **(b) After the firing test.**

Figure 13 Image analysis of Test DNT-2 in Ref. [8].

In addition, a firing test without active cooling (Test NC) was performed with the motor described in this work at the operative condition of Test 5. A nozzle erosion of 0.0125 mm/s was observed. Figure 14 compares the temperatures measured at 3 and 7 mm from the throat in these two tests. Test 5 exhibited temperatures 400 K lower than Test NC at both positions. Note that Test 5 featured a higher heating rate in the first 2 seconds, damped and controlled by the cooling system. Figure 15 displays the nozzle of Test 5 before and after the firing test. The throat remained unaltered, and the structural integrity of the graphite was conserved. Indeed, no cracking was observed from a superficial inspection of the inner and outer graphite surfaces. The nozzle may be further reused for additional firing tests, making the propulsion system more reliable for multiple ignitions, another crucial feature for space missions.

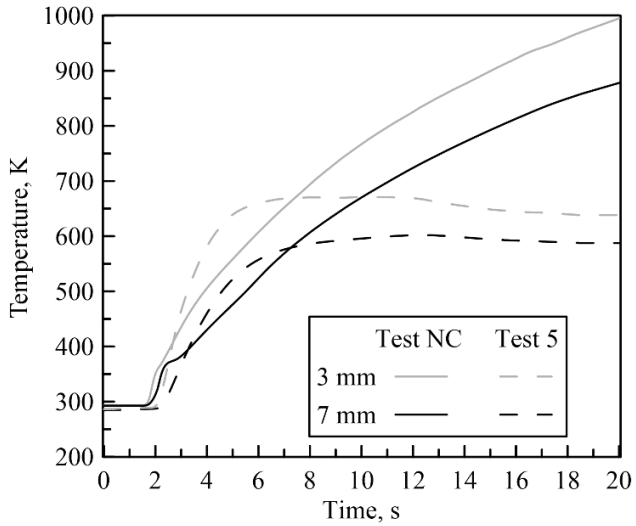

Figure 14 A comparison of the temperature signals at 3 and 7 mm from the throat.

(a) Before the firing test. **(b) After the firing test.**

Figure 15 Image analysis of Test 5.

In summary, the implementation of regenerative cooling leads to benefits and drawbacks, which are listed here:

- Pros:

1. Suppression of nozzle erosion and improvement of motor performance in terms of thrust and specific impulse.
2. Greater reusability with the capability of multiple ignitions at the same performance.
3. Self-handling of the chamber heat fluxes and elimination of heavy TPS for the thermal insulation of the satellite from the nozzle.

- Cons:
  1. Lower repeatability and control in the test conditions because of the thermal coupling of the feeding line with the combustion chamber.
  2. Higher complexity of the overall propulsion system due to the introduction of additional pipes and helical printed channels.

3.3 Multiphase Flow Identification and Results

In this section, the vaporization of the subcritical oxygen is discussed with the aim to estimate the trend of the amount of gasified coolant among the tests. The weak sensitivity of the mass flow rate to the pressure drop displayed in Figure 12b is investigated. Observing Eq. (13), two quantities may change among the tests to realize different mass flow rates in addition to Δp: the friction coefficient and the fluid density. Figure 16 represents the coolant inlet and outlet conditions of the above-presented firing tests. Because the outlet state is beyond the oxygen vapour curve, density variations due to coolant gasification are assumed to be more significant than the variations of the friction coefficient in the characteristic range of the Reynolds number of our tests. For this reason, density variations are taken into account in our analysis, while the friction coefficient is assumed to be constant and equal to 0.025 (corresponding to a relative roughness of 0.1, as shown in Figure 5).

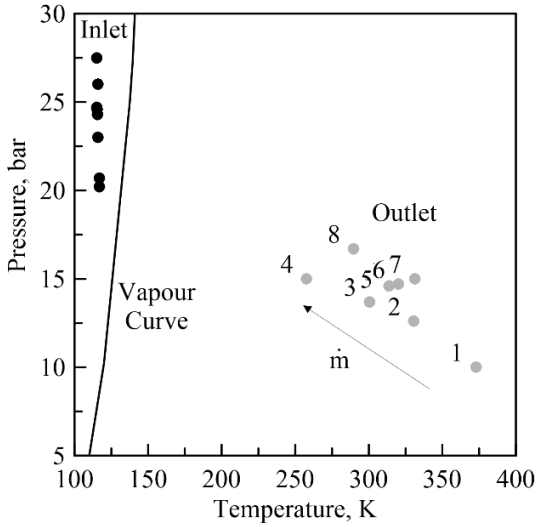

Figure 16 A representation of the inlet and outlet coolant pressure and temperature.

3.3.1 Qualitative Description of the Multiphase Flow

A qualitative description of the multiphase flow regime developed in the channels is given here to improve the understanding of the quantitative results shown in the next subsections. A summarizing sketch of the coolant flow field inside the helical channel is displayed in Figure 17, which depicts the coolant phase change (or boiling) along the heated channel and the corresponding multiphase regimes. When the coolant flows inside the channels from the inlet, the nucleate boiling is

triggered because the nozzle temperature at the cold side is hundreds of Kelvin higher than the saturation temperature of the liquid oxygen. The formation of bubbles is promoted by temperature increases and pressure drops. On the other hand, nucleating bubbles are inhibited by the dynamic pressure exerted by the liquid on the bubble surface, which increases with the coolant mass flow rate. When the bubbles grow enough, they coalesce so much that the multiphase flow regime switches from bubby to annular. When a considerable amount of vapour is formed, making it difficult for the liquid to continuously wet the surface to receive heat from the surface, a detrimental reduction of the exchanged heat flux with the coolant, refered to as "dry-out," is observed. Dry-out is supposed to not be symmetrical along the axis of the channel cross-section for two reasons: the coolant is heated only on one side, and the cooling system is made by helical channels, in which the liquid coolant is pushed on the channel cold wall by the centrifugal forces. For this reason, the complete coolant dry-out is distinguished from the dry-out onset, which occurs earlier.

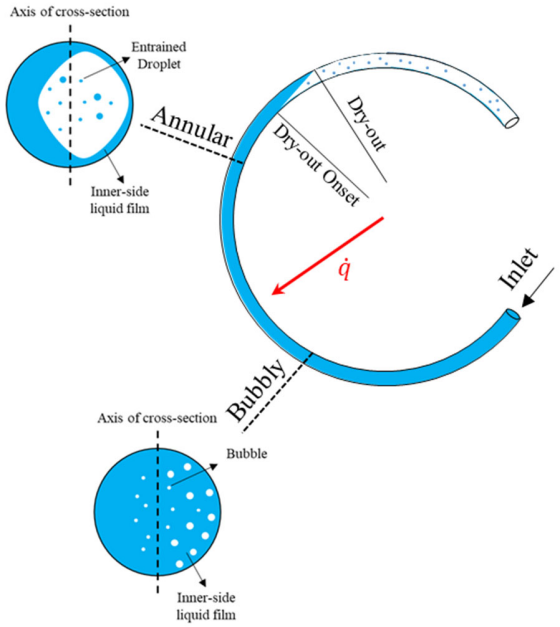

Figure 17 Sketch of the coolant flow field inside the helical channel.

Dry-out was studied for cooling applications because its occurrence at critical points may lead to the thermal failure of the engine. In these cases, the energy developed by the engine is unrelated to the capability of the cooling system to extract heat flux, which is not true for regenerative cooling. On one hand, the coolant gasification promotes the dry-out, dropping the cooling performance. On the other hand, it decreases the system mass flow rate, limiting the total amount of heat transferred from the combustion gases to the throat. In short, the coolant gasification reduces both the coolant heat transfer coefficient on the cold side and the heat transfer coefficient of the combustion gas on the hot side. So, the total propulsion system turns out to be self-regulating, smoothing critical thermal issues; however, this makes the motor performance less predictable and extremely sensitive to the thermal environment developed in the chamber.

3.3.2 Coolant Density, Void Fraction and Vapour Quality

Once a friction coefficient equal to 0.025 is imposed, the average fluid density, void fraction, and vapour quality can be obtained by Eq. (2) and Eq. (5). These two quantities define the amount of gasified coolant in terms of volume and mass,

respectively. Figure 18 displays their trend with the coolant mass flow rate per channel. The average density increases linearly from 38 to 200 kg/m^3, while the average void fraction decreases linearly from 0.98 to 0.83. The vapour quality rapidly drops from 0.65 to 0.27 between 2.5 and 4.5 g/s; beyond which it decreases slightly further from 0.27 to 0.20. Therefore, coolant vaporization is encouraged at low mass flow rates. Note that these findings are in line with Figure 16, where the hottest outlet temperatures are recorded in the tests with the lowest mass flow rates and, consequently, the lowest mixture specific heat (see Figure 19). Observing Figure 12b, from a comparison of Test 3 with Test 4 and 5, a lower tank pressure is required to obtain approximately the same mass flow rate because Test 3 has a lower vaporization degree. Indeed, this test exhibited a specific impulse around 1500 m/s, while the latter around 1900 m/s suggests that hotter flame temperatures have been developed (see Table 1).

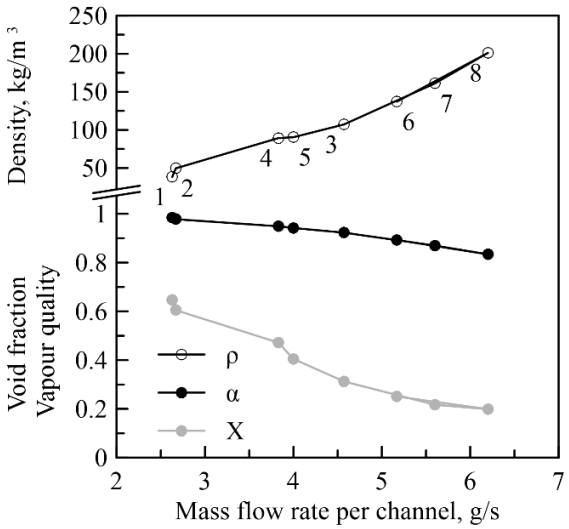

Figure 18 Average coolant density, void fraction and vapour quality computed by Eq. (2) and Eq. (5).

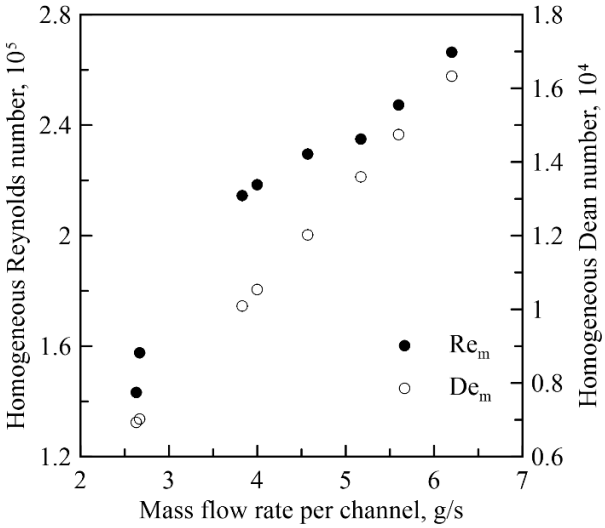

Figure 19 Average mixture specific heat vs coolant mass flow rate.

Now, that all the main multiphase quantities can be evaluated, a qualitative evaluation of the flow regime achieved in the cooling system is performed. Although no flow regime maps for cryogenic oxygen in helical channels are available in the literature, some considerations and comparisons can be made with the existing literature. Comparing with classic horizontal

flows, the occurrence of the bubbly to annular regime transition is anticipated with increasing swirl intensity [26]. A generalized flow regime map for any swirl angle with an air-water mixture is shown in Ref. [27]. In addition, Mandhane et al. proposed correction parameters for the adaptation air-water regime maps for any kind of fluid [28]. The data obtained in the test campaign have been compared with the adapted regime map for the current experimental case. Figure 20 shows superficial gas velocity versus the liquid velocity compared with the bubbly to annular boundary. All the data largely falls in the annular zone; this analysis, together with the evaluated average void fraction over 0.8, ensures the occurrence of the transition from the bubbly regime to the annular one in all the tests [29]. Finally, Figure 21 displays the characteristic homogeneous Reynolds and Dean numbers in our tests. The former is ranged between $1 \cdot 10^5$ and $3 \cdot 10^5$, while the latter is ranged $4 \cdot 10^3$ and $2 \cdot 10^4$ typical of turbulent rotating flows. The main quantities are listed in Table 2.

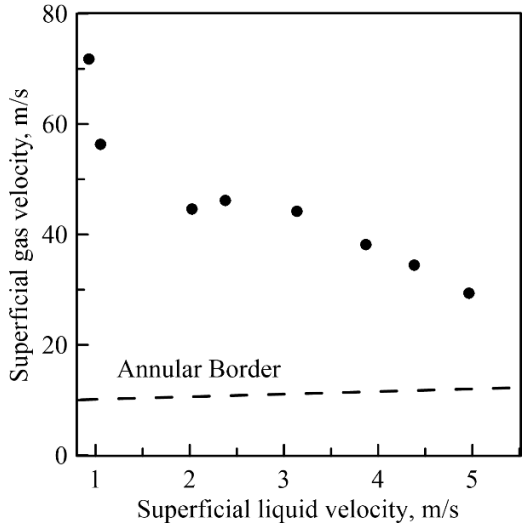

Figure 20 Superficial gas velocity versus superficial liquid velocity compared with the bubbly to annular boundary generalized to swirling oxygen flows.

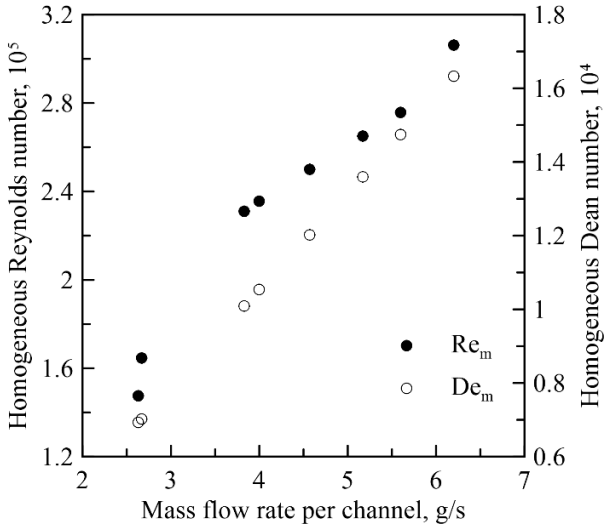

Figure 21 Homogeneous Reynolds and Dean number among the firing tests.

Table 2 Calculated density, void fraction and vapour quality.

Test	Average density, kg/m^3	Average void fraction	Average vapour quality
1	38.41	0.985	0.647
2	49.60	0.978	0.605
3	107.12	0.923	0.313
4	89.27	0.943	0.472
5	90.41	0.943	0.405
6	137.11	0.893	0.251
7	161.08	0.870	0.217
8	201.10	0.834	0.199

3.3.3 Gas Heat Transfer Coefficient and Coolant Heat Transfer Coefficient

Figure 22 displays the throat nozzle temperatures on the hot and cold sides. The tests with low cooling performance at the throat are promptly recognized by the small temperature drop from the hot to the cold sides. T_{wh} varies between 600 and 750 K with a single peak of 900 K for Test 4, while, on the other hand, T_{wc} is consistently below 525 K. Regardless, the temperature conditions required for the nozzle erosion are not reached in any test. All the calculated quantities are summarized in Table 3.

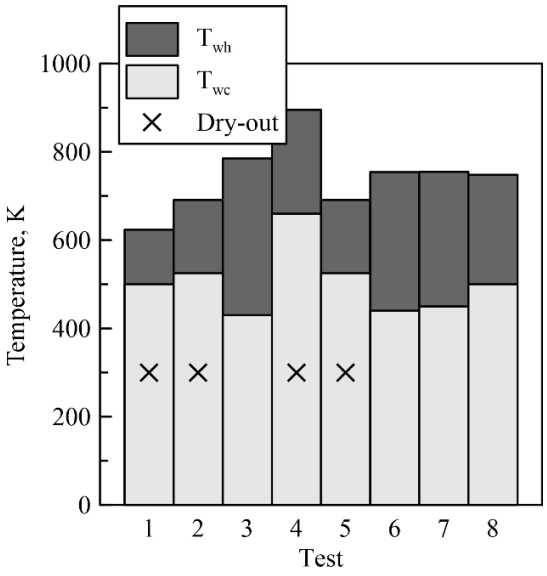

Figure 22 Wall temperature at the throat at the cold side.

Table 3 Calculated density, void fraction, vapour quality and mixture properties.

Test	Hot Temperature, K	Cold Temperature, K	Gas Heat Coefficient, W/m^{2}K	Coolant Heat Coefficient, W/m^{2}K
1	624	500	984	2636
2	691	525	1220	1777
3	785	430	1601	6612
4	894	660	1161	2360
5	690	525	1120	2633
6	754	449	1645	6263
7	754	450	1547	5886
8	748	500	1751	5230

The heat transfer results at the nozzle throat obtained by the equations described in Subsection 2.1.2 are described here. Regarding the gas heat transfer coefficient, the well-known Bartz's correlation is one of the most used, which, written in terms of the total mass flow rate, is given by [30]

$$h_g = \left[\frac{0.026}{D_t^{0.2}}\left(\frac{\mu^{0.2}c_p}{\mathrm{Pr}^{0.6}}\right)\left(\frac{\dot{m}_{tot}}{A_t}\right)^{0.8}\right]\left(\frac{A_t}{A}\right)^{0.9}\sigma$$
$$\sigma = \left\{\left[\frac{1}{2}\frac{T_{w,g}}{T_0}\left(1+\frac{\gamma-1}{2}M^2\right)+\frac{1}{2}\right]^{0.68}\left[1+\frac{\gamma-1}{2}M^2\right]^{0.12}\right\}^{-1} \quad (14)$$

Where all the quantities are evaluated at the nozzle throat, and the thermodynamic properties are assessed by the software CEA as a function of mixture ratio and the injection pressure [31]. Although the chamber pressure should be used in the calculation, the error made by using the injection pressure is negligible, since the chemical equilibrium calculations are mostly sensitive to the mixture ratio. Figure 23 represents the gas heat transfer coefficient with the total mass flow rate. A correlation law of h_g with the total mass flow rate is given,

$$h_g = 138.53\dot{m}_{tot}{}^{0.76} \quad (15)$$

As shown, h_g increases with $\dot{m}_{tot}$ with the power of 0.76 close to 0.80 of Eq. (14) from around 900 to 1800 W/m^{2}K. In addition, the experimental h_g is in average the 16% of that calculated by the above equation.

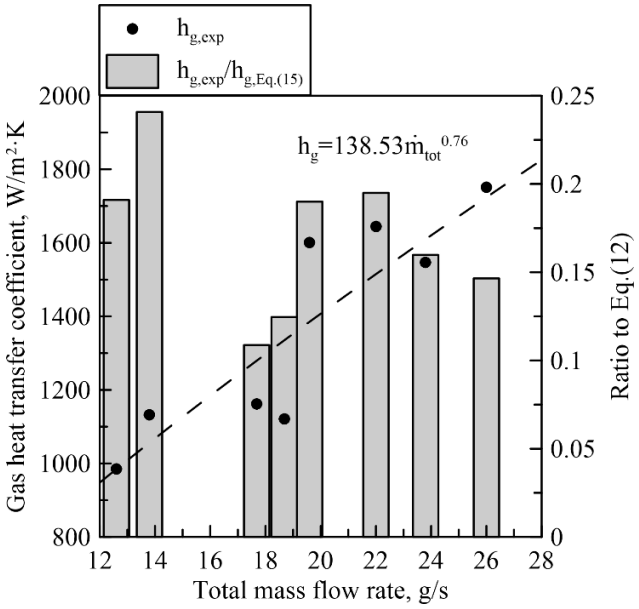

Figure 23 Hot gas heat transfer coefficient vs the total mass flow rate.

The liquid heat transfer coefficient at the nozzle throat strongly changes with the coolant mass flow rate, as shown in Figure 24a. It can be observed that h_c decreases from 7000 to 4800 W/m^{2}K for mass flow rates higher than 4.5 g/s, and it is approximately constant around 2500 W/m^{2}K for lower values. On the other hand, h_c increases with the average void fraction $\bar{\alpha} = 0.92$, while, after this threshold, a drastic drop of h_c is observed, and no trend is detected with $\bar{\alpha}$ and the mass flow rate. This behaviour is ascribed to the occurrence of the dry-out phenomenon along the cooling channel. The lowest value of h_c is observed in Test 4, which exhibited the highest nozzle temperatures and the lowest outlet temperatures. It is worth noting that h_c at the nozzle throat appears to be a function of the gas fraction rather than the coolant mass flow rate for void fractions lower than 0.92.

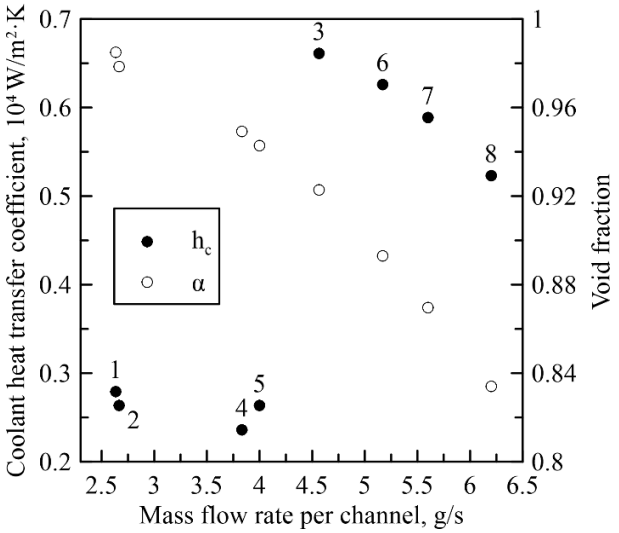

Figure 24 Coolant heat transfer coefficient vs coolant mass flow rate and void fraction.

Figure 24 represents an increasing trend of coolant heat transfer coefficient with the vapor quality in Tests 3, 5, 6 and 7, typical of annular flow regimes with the liquid phase deposited on the wall of the channel and dry-out; in this case, the

macroconvective heat transfer mechanism strongly increases with the vapour quality until the occurrence of dry-out [32, 33, 34]. The achievement of a simple and fast correlation law for the heat transfer coefficient may be useful for users interested in low-order models devoted to cooling design like that shown in our previous work [19]. Neglecting the microconvective mechanism associated with bubble nucleation and growth, the heat transfer coefficient can be modelled in the following way [35]:

$$h_c = \begin{cases} h_{conv,l}F, & 0 < \alpha \leq 0.92 \\ h_{conv,l}, & \alpha = 0 \; and \; \alpha > 0.92 \end{cases} \tag{16}$$

Where $h_{conv,l}$ is the convective heat transfer coefficient of the only liquid phase and F represents the enhancement due to the coolant boiling. $h_{conv,l}$ is mainly dependent on the liquid Dean number, while the parameter F is dependent on the Martinelli parameter, which in turn is related to the vapor quality. The total heat transfer coefficient is independent of the vapour quality when vaporization is not triggered or dry-out occurs ($\alpha = 0$ and $\alpha > 0.92$); on the other hand, the convective heat transfer is enhanced by the coolant gasification when $0 < \alpha \leq 0.92$. Referring to the modified Dittus-Boelter correlation for coiled tube heat exchangers, $h_{conv,l}$ on the hot side is given by [36]:

$$h_{conv,l} = 0.343 De_l^{0.43} Pr^{1.06} k_c / D_h \tag{17}$$

Then, F can be evaluated by Eq. (16) and it was represented in Figure 25 with the corresponding vapour quality. For the sake of convenience, assuming a linear trendline enforced to intersect the y-axis at $F = 1$ for $X = 0$, an expression of F as function of X is obtained:

$$F = 1 + 13.09\, X \tag{18}$$

Now, Eq.(16) can be revised as:

$$h_c = \begin{cases} 0.343 De_l^{0.43} Pr^{1.06} k_c / D_h \; (1 + 13.09\, X), & \alpha \leq 0.92 \\ 0.343 De_l^{0.43} Pr^{1.06} k_c / D_h, & \alpha > 0.92 \end{cases} \tag{19}$$

As shown, although Test 8 was performed with a larger mass flow rate than Test 3, the convective heat transfer of the latter is amplified by around 5 times for the higher gasification rate. Note that, assuming the same heat flux per unit of mass flow rate, the gasification rate decreases with the mass flow rate according to the suppression mechanism introduced by Chen [37,38]. Indeed, the pressure force exerted by the liquid on the bubble interface suppresses nucleating bubbles, delaying the gasification mechanism. In conclusion, an optimum range of operative mass flow rates exists close to 4.5 g/s per channel in this application: low mass flow rates promote dry-out, leading to a drastic drop in cooling performance, while large mass flow rates discourage boiling and the corresponding heat transfer enhancement.

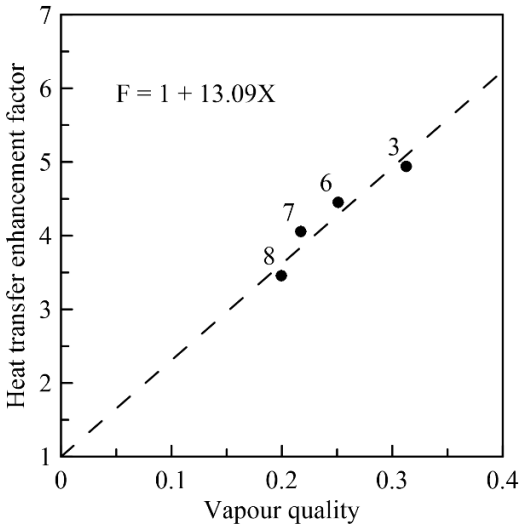

Figure 25 Heat transfer enhancement factor vs vapour quality.

3.3.4 Impact of the Friction Coefficient

This subsection shows the effect of the choice of the friction coefficient on the main results. A lower and upper boundary of f is identified at 0.017 and 0.033, respectively. For f below 0.017, unphysical vapor qualities higher than 1 are obtained. For f above 0.033, the condition of no vaporization is obtained in some tests, which is in contrast with our findings. Indeed, different tank pressure–mass flow rate trends should be observed for tests with no vaporization. A parametric analysis has been performed, assuming f equal to 0.017, 0.025 and 0.033.

Figure 26a displays the vapour quality with the coolant mass flow rate. Higher levels of vapour quality are computed for smaller friction coefficients. The trend of the vaporization is linear with the friction coefficient; indeed, a reduction of f by 40% involves a drop of 40% in the vapour quality. An increase in the vaporization leads to a decrease in the mixture coolant viscosity; accordingly, Figure 26b shows the rise of the homogeneous Reynolds number for smaller f because of the drop in the coolant viscosity. For the highest mass flow rate, Re_m only increases from around 2 to $3 \cdot 10^5$ in the considered friction coefficient range. Figure 26c shows the comparison of the tests with the above-mentioned multiphase map. All the data still fall in the annular regime, showing that the choice of the friction coefficient does not affect all the comments about the evolution of the coolant flow along the channel. Finally, Figure 26d displays the coolant heat transfer coefficient with the void fraction. The $\bar{\alpha}$ corresponding to the onset of the dry-out shifts from 0.85 to 0.95, while the highest void fraction changes from around 0.88 to 0.99.

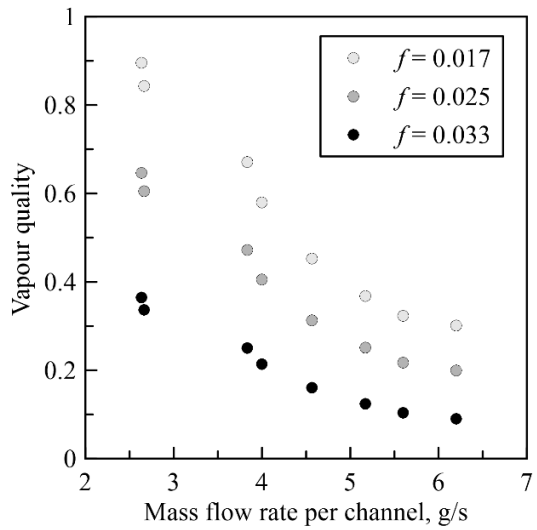

(a) Vapour quality.

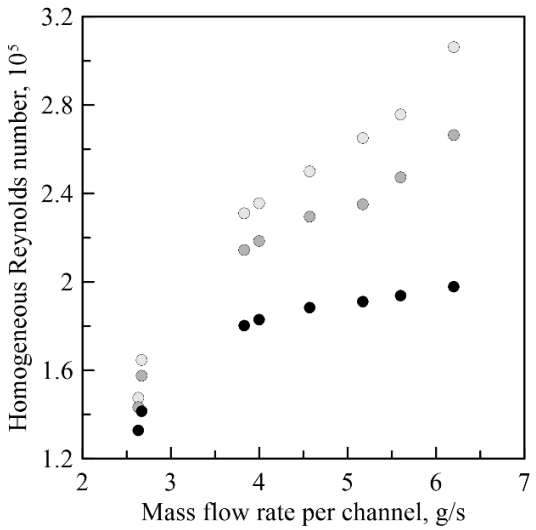

(b) Homogeneous Reynolds number.

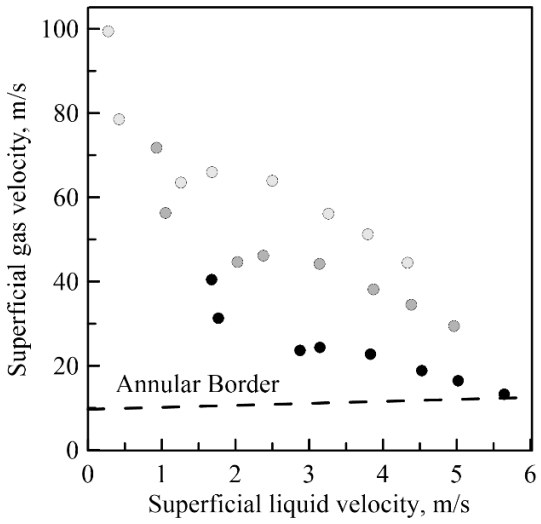

(c) Flow regime map.

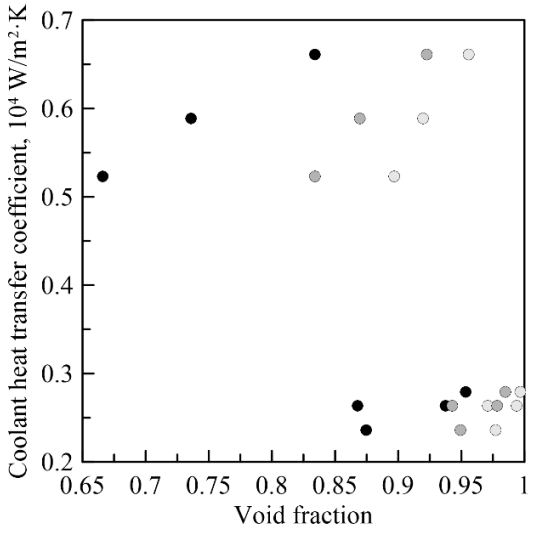

(d) Coolant heat transfer coefficient.

Figure 26 Parametric analysis of the main multiphase quantities varying the reference friction coefficient.

4 Conclusions

The results of an experimental campaign for the investigation of the cooling performance of a regenerative cooling system in hybrid rocket engines to discourage nozzle erosion and alleviate the requirement for heavy thermal protection systems are presented in this paper. The technological novelty introduced in this work lies in the active thermal control of the harsh heat fluxes developed in a graphite nozzle throat using the oxidizer as a coolant in a hybrid rocket configuration, which has typically relied solely on thermal insulation. Eight firing tests have been performed in different operating conditions, varying the upstream pressure, in order to investigate the capability of the concept for several flow rates and thrust levels. As a result, the following conclusions can be made.

An average temperature rise of around 200 K with a jump pressure of 10 bar was observed along the channels among the tests. Nozzle erosion was successfully suppressed in all the tests, exhibiting a meximum temperature of around 800 K at 3 mm from the throat surface in only one case.

The weak dependency of the mass on the pressure jump suggested to the authors the crucial role of coolant gasification in motor operative conditions. The vaporization results have been indirectly obtained by assuming a reference friction coefficient of 0.025. The average vapour quality decreased from 0.6 to 0.2 by increasing the mass flow rate from 8 to 18.6 g/s; accordingly, the coolant density increased from 40 to 200 kg/m^3. From the comparison of the results with the multiphase regime maps, the annular regime was recognized as the main characteristic multiphase regime.

Two different trends have been observed by varying the coolant mass flow rate. For mass flow rates per channel higher than 4.5 g/s, the coolant heat transfer coefficient decreases with the mass flow rate, from around 7000 to 5000 W/m^{2}K, and increases with the vapour quality; for lower mass flow rates or void fractions higher than 0.92, the coolant heat transfer coefficient is approximately constant around 2000 W/m^{2}K. Therefore, in this application, an optimum range of operative mass flow rates was found to be roughly 4.5 g/s per channel.

Finally, the benefits and drawbacks of the proposed regenerative cooling are clarified. The main pros are the self-handling of the heat fluxes transferred from the combustion gases to the graphite nozzle, ensuing the total suppression of nozzle erosion and higher reusability of the overall propulsion system. The main cons are the lower repeatability of the firing tests due to the coupling of the feed system with the combustion chamber and the additional complexity involved by 3D-printed helical channels.

5 Acknowledgement

This research was supported by the Ministry of Education, Science, Sports and Culture Grants-in-Aid for Young Scientists 20K14946, 2020 and Japan Society for the Promotion of Science (JSPS).

6 References

[1] T. Shimada, C. Carmicino, A. Karabeyoglu, Hybrid Rocket (Volume II), Aerospace, 9(5) (2022) 233, https://doi.org/10.3390/aerospace9050233

[2] C. Carmicino, Advances in Hybrid Rocket Technology and Related Analysis Methodologies, Aerospace, 6(12) (2019) 128, https://doi.org/10.3390/aerospace6120128

[3] D. Altman, A. Holzman, Overview and History of Hybrid Rocket Propulsion. Fundamentals of Hybrid Rocket Combustion and Propulsion, edited by K. Kuo, M. Chiaverini, AIAA Progress in Astronautics and Aeronautics, 218 (2007), 1–36, https://doi.org/10.2514/5.9781600866876.0001.0036

[4] K. Kuo, M. Chiaverini, Challenges of Hybrid Rocket Propulsion in the 21st Century, Fundamentals of Hybrid Rocket Propulsion, edited by M. Chiaverini, and K. Kuo, AIAA Progress in Astronautics and Aeronautics, 218 (2006) 593–638.

[5] X. Jiang, H. Tian, G. Tan, S. Zhao, G. Cai, Experiments of Ablation Characteristics for Different Nozzle Materials and Transient Simulations on Thermochemical Erosion in Hybrid Rocket Motors, Acta Astronaut., 212 (2023) 455-466, https://doi.org/10.1016/j.actaastro.2023.08.027

[6] B. Heath, M. Ewing, Uncertainty in Modeling Ablation Heat Transfer in Rocket Nozzles, 38 (1) (2024) 109-116, https://doi.org/10.2514/1.T6856

[7] L. Kamps, Y. Saito, R. Kawabata, M. Wakita, T. Totani, Y. Takahashi, H. Nagata, Method for Determining Nozzle-Throat-Erosion-History in Hybrid Rockets, J. Propuls. Power, 33(6) (2017) 1369-1377, https://doi.org/10.2514/1.B36390

[8] L. Kamps, S. Hirai, K. Sakurai, T. Viscor, Y. Saito, R. Guan, H. Isochi, N. Adachi, M. Itoh, H. Nagata, Investigation of Graphite Nozzle Erosion in Hybrid Rockets Using Oxygen/High-Density Polyethylene, J. Propuls. Power, 36 (3) (2020) 423–434, https://doi.org/10.2514/1.B37568

[9] D. Bianchi, M. T. Migliorino, M. Rotondi, L. Kamps, H. Nagata, Numerical Analysis of Nozzle Erosion in Hybrid Rockets and Comparison with Experiments, J. Propuls. Power, 38 (3) (2022) 389–409, https://doi.org/10.2514/1.B38547

[10] C. Zhang, H. Gao, J. Zhao, G. Yao, D. Wen, Working State Map of Hydrocarbon Fuels for Regenerative Cooling, Propuls. Power Res., 12 (2) (2023) 199-211, https://doi.org/10.1016/j.jppr.2023.05.002

[11] J. Wang, H. Jin, H. Gao, D. Wen, Cooling Capacity Optimization of Hydrocarbon Fuels for Regenerative Cooling, Appl. Therm. Eng., 200 (2022) 117661, https://doi.org/10.1016/j.applthermaleng.2021.117661

[12] K. Tian, P. Yang, J. J. Klemeš, T. Ma, M. Zeng, Q. Wang, Effect of Pressure on Regenerative Cooling Process of Endothermic Hydrocarbon Fuel at Severe Pyrolysis Conditions, Aerosp. Sci. Technol., 138 (2023) 108357, https://doi.org/10.1016/j.ast.2023.108357

[13] I. A. Bhutto, I. Khan, M. Furqan, A. H. Alzahrani, A. A. Bhutto, A. Singh, Wall Film Cooling Mechanism in Liquid Fuel Combustion Chamber Containing Gaseous Hydrogen, Int. J. Hydrog. Energy, 52 (Part B) (2024) 246-255, https://doi.org/10.1016/j.ijhydene.2023.06.332

[14] H. G. Price, Cooling of High-Pressure Rocket Thrust Chambers with Liquid Oxygen, J. Spacecr. Rockets, 18(4) (1980) 338-343, https://doi.org/10.2514/3.57826

[15] S. Yuasa, K. Kitagawa, T. Sakurazawa, I. Kumazawa, T. Sakurai, Liquid Oxygen Vaporization Techniques for Swirling-Oxidizer-Flow-Type Hybrid Rocket Engines, Int. J. Energ. Mater. Chem. Propuls., 10(2) (2011) 155-168, https://doi.org/10.1615/IntJEnergeticMaterialsChemProp.2012001351

[16] S. D. Eilers, S. Whitmore, Z. Peterson, US Patent No. US2014/0026537A1, 2014.

[17] H. Nagata, T. Uematsu, M. Ito, A. Kakikura, Y. Kaneko, K. Mori, N. Murai, T. Sato, R. Mitsuhashi, T. Totani, Development of 90 kgf Class CAMUI Hybrid Rocket for a CanSat Experiment, Trans. Jpn. Soc. Aeronaut. Space Sci., 7(26) (2009) Tu_1-Tu_5, https://doi.org/10.2322/tstj.7.Tu_1

[18] Anon., Isotropic Graphite: Typical Properties, https://www.tokaicarbon.co.jp/en/products/fine_carbon/pdf/Isotropic_graphite.pdf

[19] G. Gallo, L. Kamps, H. Shota, C. Carmicino, H. Nagata, One-Dimensional Modelling of the Nozzle Cooling with Cryogenic Oxygen Flowing through Helical Channels in a Hybrid Rocket, Acta Astronaut., 210 (2023), https://doi.org/10.1016/j.actaastro.2023.05.013

[20] W. Rasband, ImageJ, U.S. National Institutes of Health, Bethesda, MD, 1997.

[21] D. R. H. Beattie, P. B. Whalley, A Simple Two-Phase Frictional Pressure Drop Calculation Method, Int. J. Multiph. Flow, 8 (1982) 83-87, https://doi.org/10.1016/0301-9322(82)90009-X

[22] G. Su, D. S. Viswanath, Generalized thermodynamic properties of real gases: Part II. Generalized Benedict-Webb-Rubin equation of state for real gases, AIChE Journal, 11 (2) (1965) 205-207, https://doi.org/10.1002/aic.690110207

[23] B. A. Younglove. Thermophysical Properties of Fluids. I. Argon, Ethylene, Parahydrogen, Nitrogen, Nitrogen Trifluoride, and Oxygen, Journal of Physical and Chemical Reference Data, 14 (619) (1985) 1-353, https://doi.org/10.1063/1.555731.

[24] H. J. M. Hanley, R. D. McCarty, W. M. Haynes, The viscosity and thermal conductivity coefficients for dense gaseous and liquid Argon, Krypton, Xenon, Nitrogen and Oxygen, Journal of Physical and Chemical Reference Data, 3 (1979) 979-1017, https://doi.org/10.1063/1.3253152

[25] A. I. Lutcov, V. I. Volga, B. K. Dymov, Thermal Conductivity, Electric Resistivity and Specific Heat of Dense Graphite, Carbon, 8 (6) (1970) 753-760, https://doi.org/10.1016/0008-6223(70)90100-4

[26] Y. Rao, Z. Liu, S. Wang, L. Li, Numerical Simulation on the Flow Pattern of a Gas–Liquid Two-Phase Swirl Flow, ACS Omega, 7 (2022) 2679-2689, https://doi.org/10.1021/acsomega.1c05144

[27]L. Liu, B. Bai, Flow regime identification of swirling gas-liquid flow with image processing technique and neural networks, Chem. Eng. Sci., 199 (2019) 588-601, https://doi.org/10.1016/j.ces.2019.01.037

[28] J. M. Mandhane, G.A. Gregory, K. Aziz, A Flow Pattern Map for Gas-Liquid Flow in Horizontal Pipes, Int. J. Multiphase Flow, 1 (1973) 537-553, https://doi.org/10.1016/0301-9322(74)90006-8

[29] J. J. Jeong, Constitutive equations, Thermal-Hydraulics of Water Cooled Nuclear Reactors, Woodhead Publishing, Chapter 9, 2017, pp. 549-594, https://doi.org/10.1016/B978-0-08-100662-7.00009-9

[30] D. R. Bartz, A Simple Equation for Rapid Estimation of Rocket Nozzle Convective Heat Transfer Coefficient, Jet Propuls., 27(1) (1957), https://doi.org/10.2514/8.12572

[31] S. Gordon, B. J. McBride, Computer Program of Complex Chemical Equilibrium Compositions and Applications, NASA Reference Publication 1311, 1994.

[32] P. A. Kew, K. Cornwell, Correlations for the Prediction of Boiling Heat Transfer in Small-Diameter Channels, Appl. Therm. Eng., 17 (1997) 705-715, https://doi.org/10.1016/S1359-4311(96)00071-3

[33] M. Matkovic, A. Cavallini, D. Del Col, L. Rossetto, Experimental Study on Condensation Heat Transfer Inside a Single Circular Minichannel, Int. J. Heat Mass Transf., 52 (9-10) (2009) 2311–2323, https://doi.org/10.1016/j.ijheatmasstransfer.2008.11.013

[34] Y. Qiu, T. Vo, D. Garg, H. Lee, C. R. Kharangate, A Systematic Approach to Optimization of ANN Model Parameters to Predict Flow Boiling Heat Transfer Coefficient in Mini/Micro-Channel Heatsinks, Int. J. Heat Mass Transf., 202 (2023) 123728, https://doi.org/10.1016/j.ijheatmasstransfer.2022.123728

[35] J. C. Chen, Correlation for Boiling Heat Transfer to Saturated Fluids in Convective Flow, Ind. Eng. Chem. Process Des. Dev., 5 (1966) 322–329, https://doi.org/10.1021/i260019a023

[36] M. R. Salimpour, Heat Transfer Coefficients of Shell and Coiled Tube Heat Exchangers, Exp. Therm. Fluid Sci., 33 (2) (2009) 203–207, https://doi.org/10.1016/j.expthermflusci.2008.07.015

[37] N. Shah, H. B. Mehta, J. Banerjee, Experimental Investigations on a Novel Instability Suppression Mechanism for Subcooled Flow Boiling in Microchannel Heat Sink, Appl. Therm. Eng., 239 (2024) 122006, https://doi.org/10.1016/j.applthermaleng.2023.122006

[38] L. Chen, P. Zhou, R. Huang, X. Han, S. Hua, Z. Li, L. Gao, , Experimental investigation on the suppression factor in subcooled boiling flow, Appl. Therm. Eng., 135 (2018) 549-558, https://doi.org/10.1016/j.applthermaleng.2018.02.026.